ChemComm
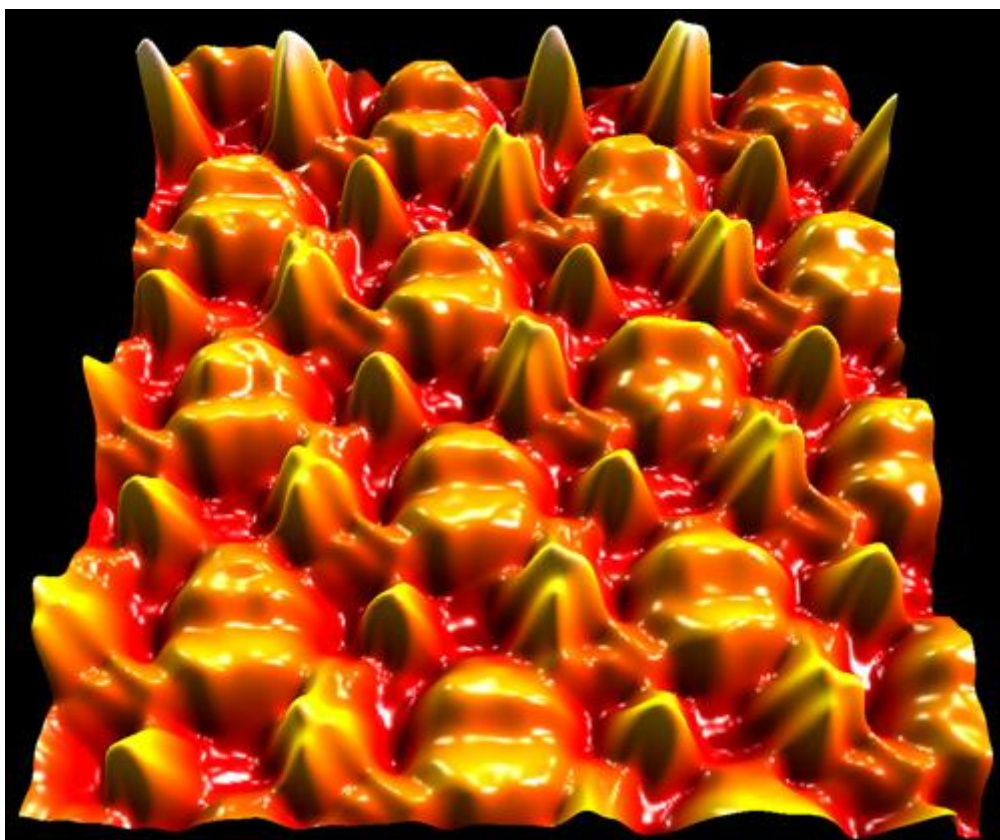
This article is part of the

Molecule-based Surface Chemistry web themed issue

Guest Editors include Steven De Feyter, Federico Rosei & Dmitrii Perepichka

Please visit the website to access the other articles in this issue:-
http://www.rsc.org/chemcomm/surfacechemistry

FEATURE ARTICLE

Single-molecule chemistry and physics explored by low-temperature scanning probe microscopy

Ingmar Swart,[a] **Leo Gross**[b] **and Peter Liljeroth**[*cd]

It is well known that scanning probe techniques such as scanning tunnelling microscopy (STM) and atomic force microscopy (AFM) routinely offer atomic scale information on the geometric and the electronic structure of solids. Recent developments in STM and especially in non-contact AFM have allowed imaging and spectroscopy of individual molecules on surfaces with unprecedented spatial resolution, which makes it possible to study chemistry and physics at the single molecule level. In this feature article, we first review the physical concepts underlying image contrast in STM and AFM. We then focus on the key experimental considerations and use selected examples to demonstrate the capabilities of modern day low-temperature scanning probe microscopy in providing chemical insight at the single molecule level.

Introduction

Since their conception, scanning probe techniques—scanning tunnelling microscopy (STM) and atomic force microscopy (AFM)—have become established as the main experimental techniques in nanoscience to obtain atomic scale structural and spectroscopic information.[1–9] Traditionally, scanning probe methods have been used to image well-defined surfaces with atomic resolution.[1,5,10] Recent advances in STM have demonstrated sub-molecular geometrical image resolution.[11–13] In addition, the spatial resolution of non-contact atomic force microscopy (NC-AFM) has increased tremendously in recent years due to the introduction of a quartz tuning fork based force detection scheme, the so-called qPlus force sensor.[14,15] The tuning fork acts as an extremely stiff cantilever that makes it possible to operate NC-AFM with sub-Ångström tip oscillation amplitudes. This is beneficial for high-resolution imaging as small amplitudes enhance the sensitivity towards short-range forces that are responsible for atomic-scale contrast. In addition, due to the stiffness of the tuning fork, it is possible to carry out simultaneous STM experiments with uncompromised performance on the same atomic location as the AFM experiments.[16,17]

In studying the electronic properties and chemistry of individual molecules, it is beneficial to electronically decouple them from their surrounding, *i.e.* the molecules should not have strong interactions with other molecules or the substrate. One of the best ways to achieve this is to study molecules adsorbed on an ultrathin film of an insulating material.[8,18–20] A film of a few monolayers (MLs) thickness provides sufficient decoupling, while still being thin enough to allow a measurable tunnelling current to flow. This makes it possible to directly image molecular orbitals of essentially isolated molecules by STM.[8,18,21] Decoupling the molecule from the metal substrate brings an additional advantage for single-molecule chemistry: it increases the life-time of the tunnelling electrons on the molecule,[18,22] which in turn increases the probability of electron-induced chemical reactions.

These advances in instrumentation and sample preparation have made it possible to carry out single-molecule synthesis and full physicochemical characterization with atomic spatial resolution using scanning probe techniques. This is the topic of our feature article. We will first introduce the basic principles behind STM and NC-AFM imaging to emphasize conceptual understanding of the relevant physics issues. Subsequently, we will use selected examples to illustrate the potential of low-temperature scanning probe techniques to study chemistry at the level of individual molecules. In particular, we will demonstrate the synthesis of a target molecule using scanning probe methods,[20] and how AFM can be used to probe the overall electron density of a molecule, revealing the atomic structure and bonds.[17]

Introduction to physical concepts

In particular on single crystal surfaces, it has been amply demonstrated that both STM and NC-AFM can be used to obtain atomic resolution images of the surface. Nevertheless, especially in the case of molecules, the actual measured

[a] *Institute for Experimental and Applied Physics, Faculty of Physics, University of Regensburg, 93053 Regensburg, Germany*
[b] *IBM Research-Zurich, 8803 Rüschlikon, Switzerland*
[c] *Debye Institute for Nanomaterials Science, Utrecht University, PO Box 80000, 3508 TA Utrecht, The Netherlands*
[d] *Department of Applied Physics, Aalto University School of Science, PO Box 15100, 00076 Aalto, Finland. E-mail: peter.liljeroth@aalto.fi*

quantity (current, force, force gradient *etc.*) should always be kept in mind in interpreting the contrast in scanning probe microscopy images. The image formation mechanisms are quite different in STM and AFM and these techniques can be used to yield complementary information on the molecule under study. In this section, we will briefly review the physical concepts responsible for contrast in STM and AFM images.

Scanning tunnelling microscopy

In the STM, the measured tunnelling current depends on the local density of electronic states (LDOS) close to the Fermi level of the sample.[23–25] Under constant current feedback, the STM tip traces approximately the constant integrated LDOS surface, since the total tunnelling current at a tip position (x,y) is given by (in the tunnelling regime, with tip-sample distance $z > 4$ Å)[23,26,27]

$$I(V_b, x, y) \propto \int_0^{eV_b} \rho_t(E - eV_b)\rho_s(E, x, y)T(E, V_b, z)\mathrm{d}E \quad (1)$$

where V_b is the bias voltage (defined as the sample bias with respect to the tip), ρ_t and ρ_s are the tip and sample DOS, respectively, E is the energy, and T is the transmission coefficient. By differentiating the tunnelling current, one obtains[27]

$$\mathrm{d}I/\mathrm{d}V_b(V_b, x, y) \propto T(eV_b, V_b, z)\rho_s(eV_b, x, y)\rho_t(0)$$

$$+ \int_0^{eV_b} \rho_s(E, x, y)\frac{\mathrm{d}[T(E, V_b, z)\rho_t(E - eV_b)]}{\mathrm{d}eV_b}\mathrm{d}E$$

$$(2)$$

Assuming an energy independent transmission function and tip DOS, we can see that the measured $\mathrm{d}I/\mathrm{d}V_b$ is directly
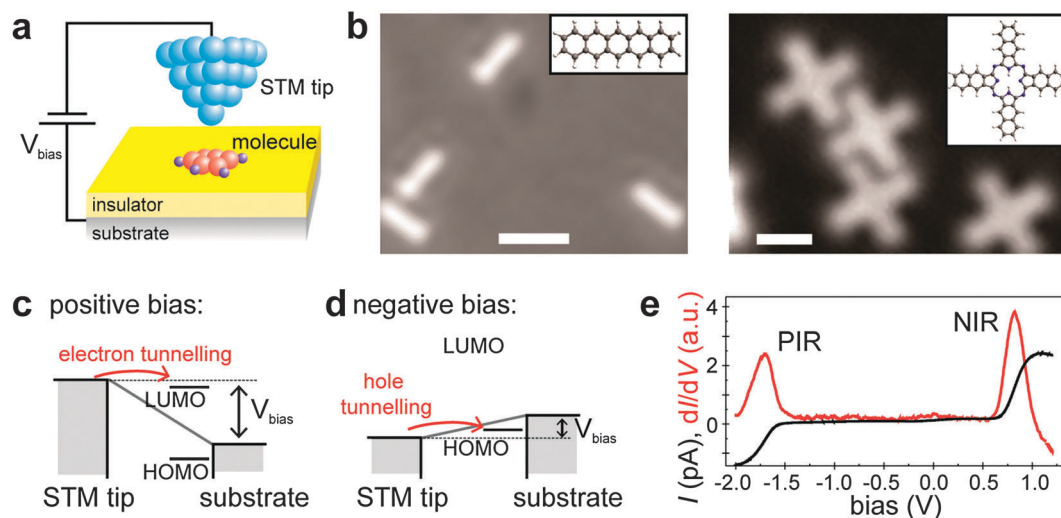
proportional to the LDOS of the sample at the position of the STM tip. This very important result forms the basis for all scanning tunnelling spectroscopy (STS) experiments, in which the $\mathrm{d}I/\mathrm{d}V_b$ signal is interpreted as being proportional to the LDOS of the sample with atomic spatial resolution. While the procedure for rigorously recovering LDOS from the measured $\mathrm{d}I/\mathrm{d}V_b$ spectra has been discussed at length in the literature,[27–29] the interpretation that $\mathrm{d}I/\mathrm{d}V_b(V_b, x, y) \propto \mathrm{LDOS}(eV_b, x, y)$ is usually sufficiently accurate when studying molecules.

What is the actual significance of the LDOS in the case of a molecular system? The microscopic interpretation of the measured LDOS in a single particle picture in terms of individual wavefunctions ψ_i at energy E_i is given by

$$\mathrm{LDOS}(eV_b, x, y) = \sum_{\delta E} |\psi_i(E_i, x, y)|^2 \quad (3)$$

where δE is the energy resolution of the experiment. The energy resolution is determined by the operational temperature (through thermal broadening of the Fermi-function), life-time and other broadening mechanisms due to the coupling of the molecule with the substrate, and the magnitude of the bias modulation used to measure $\mathrm{d}I/\mathrm{d}V_b$.[8,30–32] As the energies of individual molecular orbitals are typically well separated it is relatively straight-forward to have a sufficient energy resolution to be able to detect individual orbitals when the experiments are carried out at a low temperature. This statement holds provided that the coupling with the substrate is sufficiently small, which typically requires the use of ultrathin insulating films.

If the molecule under study is electronically decoupled from the substrate, then the system can be considered as a double-barrier tunnel junction, schematically depicted in Fig. 1a. At low bias voltages, the shape of the molecules roughly resembles their geometric structure, *e.g.* pentacene appears

Fig. 1 (a) Schematic of the double-barrier tunnel junction formed between the STM tip and a molecule on an ultrathin insulating film. (b) Constant-current STM images of pentacene (left) and naphthalocyanine (right) molecules adsorbed on NaCl(2ML)/Cu(111) acquired at low voltage (both at 0.4 V). The structures of the molecules are given in the insets. Scale bar: 20 Å. (c) and (d) positive (negative) bias voltages result in electron (hole) tunnelling through the unoccupied (occupied) molecular orbitals. (e) Measured current (black line) and differential conductance (red line) spectra of a single naphthalocyanine molecule on NaCl(2ML)/Cu(111). The peaks labelled PIR and NIR correspond to tunnelling through the HOMO (negative bias) and the LUMO (positive bias), respectively.

as a featureless rod-like protrusion and naphthalocyanine molecules appear as crosses (Fig. 1b). In this regime, the electrons tunnel directly between the tip and the metallic substrate below the molecule and the molecule simply alters the tunnelling barrier. When the bias voltage is increased, at some point the Fermi level of the tip electrode will align with one of the unoccupied orbitals of the molecule and electron tunnelling into unoccupied states of the molecule becomes possible (Fig. 1c). Conversely, at sufficiently negative bias, hole tunnelling through occupied orbitals can occur (Fig. 1d). These processes correspond to an opening of a new tunnelling channel and result in a step increase in the measured tunnelling current and a peak in the dI/dV_b signal. Such an experiment on an individual naphthalocyanine molecule is shown in Fig. 1e. Two distinct molecular resonances are observed at -1.7 V and at 0.7 V, corresponding to the positive and negative ion resonance (PIR/NIR), respectively. At these voltages, electrons predominantly tunnel sequentially through the highest occupied molecular orbital (HOMO) and the lowest unoccupied molecular orbital (LUMO), respectively.
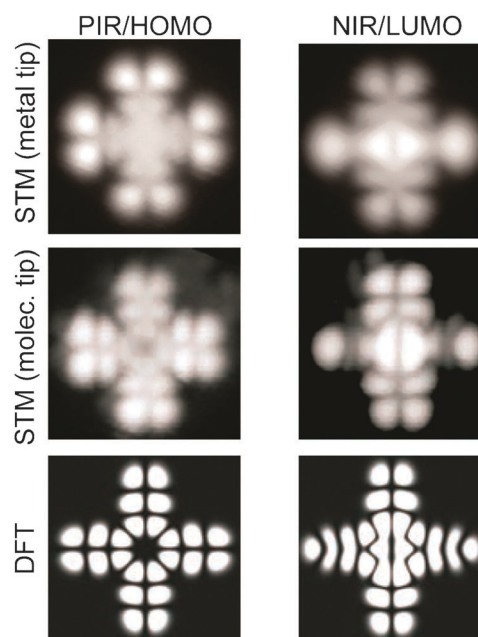
In principle, the bias voltages corresponding to the resonances directly yield the relative energies of the molecular orbitals. However, as these resonances in dI/dV_b vs. V_b spectra correspond to temporary charging of the molecule—either positively or negatively—their energies are affected by the Coulomb energy involved in adding or removing one electron. This also implies that the STM transport gap ΔV_{STM} is not equal to the HOMO–LUMO gap $\Delta E_{HOMO–LUMO}$ or the optical gap ΔE_{opt}. They are related as follows:

$$\eta \Delta V_{STM} = \Delta E_{HOMO–LUMO} + \Sigma_e + \Sigma_h = \Delta E_{opt} - J_{e,h} \quad (4)$$

where $\Sigma_{e(h)}$ is the Coulomb energy due to the addition of an electron (hole) on the LUMO (HOMO) and $J_{e,h}$ is the electron–hole attraction energy. Note that the exciton binding energy is given by $\Sigma_e + \Sigma_h - J_{e,h}$. The factor η in eqn (4) results from the potential distribution in the double-barrier tunnel junction and the finite bias drop between the molecule and the underlying metal substrate. Therefore only a factor of $\eta < 1$ of the globally applied bias drops between the STM tip and the molecule. Typically, due to the dielectric constant of the insulating films being large compared to vacuum, η is close to one and the bias voltage scale is almost equal to the real energy scale.[8,32,33]

At the voltages corresponding to the first resonance at negative and positive bias, the majority of the electrons tunnel through the HOMO and LUMO, respectively. Hence, the spatial extension of these orbitals can be mapped by simply acquiring STM images at these bias voltages. In contrast, for all other states the total current signal is the sum of the tunnel current through the individual orbitals and hence the sum of all contributing orbitals will appear in the image. This problem can be overcome by applying an ac-voltage modulation on top of the dc-bias voltage V_b and recording the spatially resolved dI/dV_b signal through lock-in detection either in the constant-current or the constant-height mode. This yields a signal that is directly proportional to the square of the wavefunction at the energy selected by the bias voltage.

Bias dependent imaging shows that at voltages corresponding to the PIR (NIR), the shape of the naphthalocyanine molecule
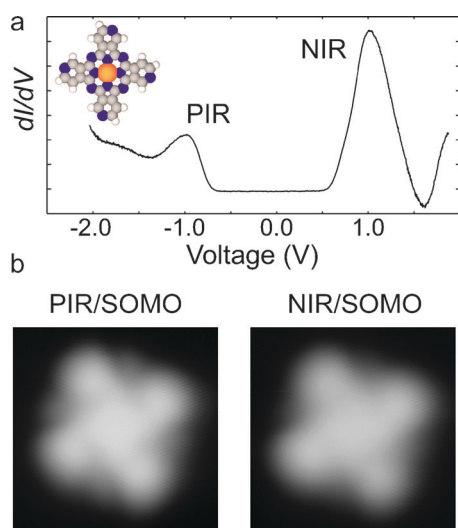

Fig. 2 STM images of naphthalocyanine on NaCl(2ML)/Cu(111) acquired at voltages corresponding to the PIR and NIR ($I = 1$ pA, $V_b = -1.6$ V (left), $V_b = 0.65$ V (right)) with clean metal and molecule-terminated tips (top and middle rows), respectively. Bottom panels show the HOMO and LUMO orbital of the free molecule, as calculated by DFT. Adapted from ref. 19. Reprinted with permission from The American Association for the Advancement of Science.

resembles that of the HOMO (LUMO) orbital of the free molecule, as obtained from density functional theory (DFT) calculations (Fig. 2). This has been observed for a variety of different molecules, demonstrating that the electronic structure of molecules adsorbed on ultrathin NaCl films is not significantly perturbed by the substrate system. As illustrated in Fig. 2 and detailed in the "Experimental methods" section, the spatial resolution of the orbitals images can be enhanced by using a molecule-modified tip apex.

When a molecule has a singly-occupied molecular orbital (SOMO) near the Fermi level (for example, when the molecule has an odd number of electrons) both electrons and holes can tunnel through this state. Hence, a resonance corresponding to the SOMO will appear at both positive and negative bias in a differential conductance spectrum.[18,34] An example is shown in Fig. 3, where the differential conductance spectrum of a negatively charged copper-tetra-azaphthalocyanine (4NCuPc) molecule is given. This molecule has a triplet ground state, and hence two SOMOs. As a result, the orbital structure of this molecule appears similar at both bias polarities. In cases that involve tunnelling through a SOMO, the STM transport gap is not related to the HOMO–LUMO gap but can be attributed solely to the Coulomb energy associated with adding or removing an electron to or from the same orbital of the complex. In summary, dI/dV_b spectroscopy and orbital imaging in the double-barrier tunnel junction geometry give detailed information on the energetic structure (energetic position and (de)localization of frontier molecular orbitals) of electronically decoupled molecules.

Finally, there are more complicated tunnelling processes that can be studied by measuring the dI/dV_b signal. For example,

Fig. 3 (a) Differential conductance spectrum of a negatively charged 4NCuPc molecule on NaCl/Cu(100). (b) STM images acquired at voltages corresponding to the PIR and NIR (I = 5 pA, V_b = −1.125 V (left), V_b = 1.35 V (right)). The molecule appears similar in both images due to tunnelling through a SOMO. A clean metal tip was used.

molecular vibrations can be studied as they give rise to the appearance of phonon replicas in the dI/dV_b spectra.[35–39] The peak spacing equals the energy of the relevant molecular vibrational mode and the replicas correspond to tunnelling through a molecular orbital and simultaneously exciting one or more molecular vibrations. Which vibrations are excited depends on the magnitude of the electron-vibration coupling for the different normal modes of the molecule. Typically, the aromatic C–C-stretch vibrations are observed to couple strongly to electrons on the delocalized molecular orbitals.[39] This type of vibrational excitation is important in, for example, driving molecular switching by inelastic tunnelling.[19,40,41]

Atomic force microscopy

As we have seen in the previous paragraph, in contrast to common belief, STM does not usually provide the atomic geometry of the molecule. In the particular case of organic molecules, where the frontier molecular orbitals are delocalized over the entire molecule, standard STM images will not achieve atomic resolution (unless performed as scanning tunnelling hydrogen microscopy (STHM)[11–13]). In addition, they give only very indirect information on the presence of charges or charge distributions. We will discuss in the next sections how the overall electron density, displaying the genuine atomic backbone of the molecule, can be probed by small-amplitude NC-AFM. This can be achieved when short-range (chemical) forces make a significant contribution to the measured signal.[14] In addition, by measuring the force as a function of the applied bias voltage, the electrostatic component of the interaction between the molecule and a biased metal tip can be measured.[16,42] This mode of operation is called electrostatic force microscopy (EFM) or Kelvin probe force microscopy (KPFM).

Atomic force microscopy naturally uses some quantity derived from the force between the AFM tip and the substrate

as the feedback parameter. We will focus here on frequency modulation NC-AFM, which is the method of choice for measurements in ultra-high vacuum. In particular, we will concentrate on the use of a quartz tuning-fork force sensor in the so-called qPlus configuration as it allows experiments with extremely small oscillation amplitudes.[14,43,44] This is very beneficial for high-resolution imaging for reasons that will become apparent in the next sections.[5,14] An extensive introduction into NC-AFM, and the qPlus sensor in general, can be found in ref. 14. The qPlus sensor consists of a quartz tuning-fork where one of the prongs is attached to the tip holder (which has high mass and is essentially fixed). A conductive tip (typically made out of tungsten or a platinum–iridium alloy) is attached to the end of the other prong and acts as an STM/AFM tip. The cantilever oscillation is detected electrically with electrodes on the tuning fork. The high force constant of the tuning fork (typically $k \approx 1800$ N m^{-1}) allows stable operation down to sub-Ångström oscillation amplitude (down to 10 pm has been achieved) without jump-to-contact or other instabilities.

In vacuum, at a large tip–sample distance the resonance frequency f of the tuning fork is f_0 (typically in the order of 30 kHz). When the sensor approaches a surface, the resonance frequency is shifted due to interaction with the surface. The frequency shift $\Delta f = f - f_0$ can be related to the tip–sample force F_{ts} as follows[14,45–48]

$$\Delta f(z) = -\frac{f_0}{2k}\left\langle\frac{\partial F_{ts}(z)}{\partial z}\right\rangle \quad (5)$$

where z is the average tip–sample distance and $\langle\partial F_{ts}(z)/\partial z\rangle$ is the average force gradient over the tip oscillation cycle

$$\left\langle\frac{\partial F_{ts}(z)}{\partial z}\right\rangle = \frac{2}{\pi A^2}\int_{-A}^{A}\frac{\partial F_{ts}(z-q)}{\partial z}(A^2 - q^2)^{1/2}\mathrm{d}q \quad (6)$$

where A is the tip oscillation amplitude. The function $(A^2 - q^2)^{1/2}$ acts as a weight function and eqn (5) and (6) show the effect of the oscillation amplitude on the measured Δf. Using small amplitudes enhances the relative contribution of short-range force gradients, which naturally leads to the highest spatial resolution. For small oscillation amplitudes, the frequency shift is approximately given by

$$\Delta f(z) = -\frac{f_0}{2k}\frac{\partial F_{ts}(z)}{\partial z}. \quad (7)$$

With the qPlus sensors, it is possible to make the oscillation amplitude sufficiently small ($A < 20$ pm) such that eqn (7) is an excellent approximation and can be used quantitatively to convert the measured frequency shift to the tip–sample force. The tip–sample force is related to the tip–sample interaction energy U_{ts} as $F_{ts} = -\nabla U_{ts}$. Integration of the tip–sample force in the z-direction yields the potential, which can be subsequently differentiated in an arbitrary direction to obtain, for example, the lateral component of the tip–sample force.[44]

There are several contributions to the total tip–sample force F_{ts}.[10,14,16,17,24,49,50] At short tip–sample distances, the Pauli exclusion principle results in a strong repulsive interaction as the electron clouds of the last tip atom and first sample atom overlap. Depending on the nature of these atoms, there might

also be attractive interactions due to the formation of a chemical bond. Van der Waals (vdW) and electrostatic interactions also contribute. At larger distances, the van der Waals interaction between the substrate and the body of the tip is important, as well as electrostatic and, possibly, magnetic interactions. As will be discussed in detail below, when the AFM tip apex is modified with small inorganic molecules, most of the short range contribution to the Δf can be accounted for by simply considering the small molecule and the molecule on the substrate, in the absence of the body of the tip and the substrate.

As we mentioned earlier, electrostatic forces can be probed by measuring the tip–sample interaction as a function of the tip–sample bias. For an isolated charge q in the tip–substrate junction (in a double-barrier geometry), the electrostatic force is given by[16,42,51,52]

$$F_{el} = \frac{1}{C_\Sigma^2} \frac{\partial C_1}{\partial z} \left(\frac{q^2}{2} + C_2 q V_b + \frac{C_2^2 V_b^2}{2} \right) + \frac{1}{2} \frac{\partial C_0}{\partial z} V_b^2 \quad (8)$$

where C_1 and C_2 are the capacitances of the tip–charge and charge–substrate junctions, $C_\Sigma = C_1 + C_2$ and C_0 the background capacitance. The peak position of the parabola F_{el} vs. V_b (or parabola Δf vs. V_b) shifts depending on the absolute value and the sign of the charge q. Single electron charge sensitivity with sub-nanometre spatial resolution of the technique was demonstrated recently, and positive, neutral, and negative atomic charge states could be distinguished.[16]

Experimental methods

In this section we will discuss various general experimental aspects associated with performing STM and AFM experiments on molecules. Most of our studies have focussed on molecules that are electronically decoupled from the substrate. One convenient way to achieve this is to use an ultrathin alkali halide film grown on a metal single crystal as the substrate. The preparation of such films is described in the section "Preparation of ultrathin insulating films". Functionalization of the tip is essential to obtain high resolution with STM and AFM. This will be discussed in the section "Preparation of tips with controlled termination for STM and AFM imaging".

Preparation of ultrathin insulating films

The physical and chemical properties of molecules are sensitive to the (local) chemical and physical environment. On metal and semiconductor surfaces, the electronic structure of adsorbed molecules is often significantly modified due to the strong electronic coupling of molecular orbitals with states of the substrate. In contrast, on insulators only van der Waals type interactions occur, and hence the electronic structure of the molecules is almost unperturbed.

Since the metal–molecule interaction is governed by the overlap of electronic states, it is sensitively dependent on distance. It has been found that insulating films of only a few atomic layers thickness are sufficient to electronically decouple molecules from the metal substrate. Such ultrathin insulating films are still thin enough to allow a measurable tunnelling current to flow. This opens up the possibility to use STM to study molecules on a weakly interacting surface.

New physical insights and phenomena, such as imaging unperturbed molecular orbitals directly in real space (vide infra),[8,19] charge-state multistability of atoms and molecules,[22,34,53,54] ambipolar charge transport,[55] vibronic spectroscopy,[37–39] spin-flip spectroscopy,[56,57] and control over the spins of atoms[58] have been discovered. A variety of insulators, such as magnesium oxide,[59] alumina,[60] noble gas atoms, and various alkali halides,[19,61] have been used to grow ultrathin films. In our work, predominantly alkali halides (NaCl, RbI) have been used since these materials form stable and atomically flat insulating films with a well-characterized and ordered geometric structure on a wide variety of surfaces.[8,19,32,61–66] In addition, alkali halides have a large band gap, which has been shown to already exist for a bilayer.[67] This provides a large energy window to study the electronic structure of molecules and to image the frontier molecular orbitals directly in real space.

NaCl (and RbI) films can be grown on single crystal Cu surfaces with various surface terminations, i.e. atomically flat surfaces, such as Cu(111) and Cu(100), as well as intrinsically stepped surfaces (Cu(311)).[21,61,63] The Cu crystals are cleaned by several standard sputtering–annealing cycles. NaCl (and RbI) are evaporated thermally from a crucible. Alkali halides evaporate in ion-pairs (or multiples thereof), leading to the correct stoichiometry of cations and anions on the surface. The rate of evaporation is monitored by a quartz crystal microbalance. On Cu(111) and Cu(100), the size of the salt islands can be tuned from a few hundred nanometres to several micrometres by controlling the temperature of the substrate. When growth temperatures slightly above room-temperature are used, micrometre sized two-monolayer thick (100)-terminated NaCl islands are formed. On top of the double layer, smaller islands of three and four monolayers grow before the coverage reaches one monolayer. At sample temperatures of 200 K, islands of one atomic layer can be grown. In all cases, the islands have exclusively non-polar edges, i.e. the edges consist of alternating cations and anions. Mono-atomic steps in the substrate can be covered by a continuous film in a 'carpet'-like fashion.[61] Due to incommensurate growth of NaCl on Cu(111) and Cu(100), many different orientations of the islands with respect to the substrate are observed.

The growth behaviour of NaCl on Cu(311) is distinctly different.[63] On this surface, atomically flat one atomic layer thick NaCl films can be grown at temperatures of ∼400 K. A NaCl bilayer only forms upon completion of the first monolayer. However, the third and fourth layers begin to grow before the second layer is complete. NaCl grows pseudo-morphically on Cu(311) with one of its polar directions parallel to the intrinsic steps of the Cu surface. In all cases, atomically resolved images of the ultrathin NaCl(100) layers can be obtained.[63,65]

Preparation of tips with controlled termination for STM and AFM imaging

A key step to increase lateral resolution using STM and AFM on molecules is the controlled termination of tips with certain atoms or molecules, a technique called tip functionalization. It is based on atomic manipulation as introduced by

Eigler and Schweizer, and one differentiates between lateral and vertical atomic manipulations.[2] Pushing, pulling and sliding atoms and molecules on a surface is referred to as lateral manipulation.[2,44,68] For the investigations of individual molecules, lateral manipulation can be used to place molecules at different adsorption sites[6,69,70] or molecular motion itself can be studied.[44,71–73] On the other hand, adsorbates can be picked up and dropped with the probe tip, which is referred to as vertical manipulation.[74,75] Vertical manipulation can also be employed for studying the contact of individual molecules with the STM tip.[76,77] Furthermore, reactions can be induced by forming or breaking molecular bonds with voltage pulses from the STM tip.[4,19,41,72,78,79]

In addition, vertical atomic manipulation can be used to functionalize tips used in scanning probe methods.[74,75] A certain atom or a molecule can be picked up by the tip by approaching it with the tip and applying a voltage pulse (a couple of volts). Using this technique, adsorbates can be transferred from the surface to the end of the tip, thus functionalizing it.
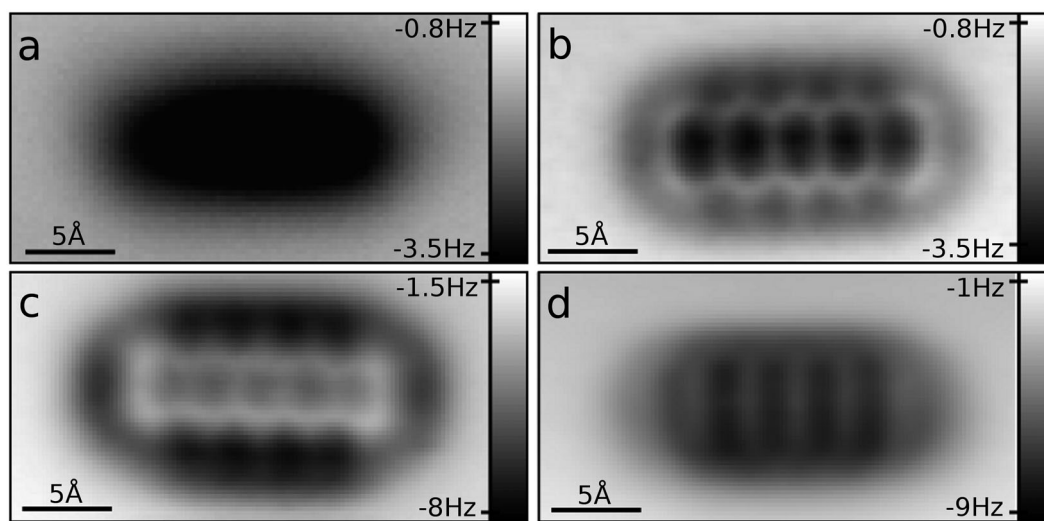
Standard tip preparation techniques for STM or AFM include heating and sputtering tips, applying voltage pulses, or bringing the tip into controlled contact with the substrate. Compared with these approaches, the tip forming by means of vertical atomic manipulation has two important advantages: first of all, it is highly reproducible and, second, the atomic identity of the foremost part of the tip is known after the functionalization, which is important information for the interpretation and theoretical corroboration of the experimental data.

The contrast obtained with SPM crucially depends on the tip functionalization and the ideal atom or molecule for tip functionalization depends on the system under investigation and on the property that should be measured (imaging electronic orbitals or geometric structure). One example is the orbital imaging of molecules on thin insulating films by STM as demonstrated by Repp et al.[8,18] It has been found that molecule-terminated STM tips can lead to enhanced image

resolution in orbital imaging.[8,17,19,80,81] One example of this is given in Fig. 2, which shows STM images of naphthalocyanine molecules acquired with a clean metal tip and with a molecule-terminated tip. Theoretical modelling of STM images has revealed that the increased resolution that can be obtained with molecule terminated tips results from the fact that molecule-terminated tips allow the molecular orbitals to be probed at an increased local density of states.[8] When using such molecule-modified tips, the precise structure of the tip apex is unknown and care has to be taken when interpreting the images. However, it has been found that picking up a single molecule such as pentacene with the STM tip does not introduce additional features in the nodal plane structure of the molecule under investigation.

Recently, great progress was made with NC-AFM, demonstrating lateral[44,82] and vertical atomic manipulations[83] also with this tool. Moreover, vertical atomic manipulation was used to functionalize the tip of an AFM with the result of imaging individual molecules with atomic resolution.[17,80] Atomic resolution on a pentacene molecule was achieved with carbon monoxide terminated tips (Fig. 4b) as well as with chloride-functionalized tips (Fig. 4c). Also in the case of NC-AFM, metal terminated tips did not show the highest resolution when imaging organic molecules, and no contrast on the atomic scale could be achieved with Cu, Ag (Fig. 4a), or Au terminations.[17] Using pentacene terminated tips that proved to be useful for orbital imaging with the STM, yielded some intramolecular contrast (see Fig. 4d) but no clear atomic resolution with NC-AFM. The best contrast with NC-AFM was observed using CO tip functionalization, which revealed all atoms and bonds within pentacene molecules.

To understand the reason for this contrast enhancement, DFT calculations were carried out.[17,84] The calculations assigned the atomic contrast to the Pauli repulsion while the longer-ranged attractive van der Waals and electrostatic forces show no atomic corrugation and give rise to the dark halo

Fig. 4 Constant-height NC-AFM images of pentacene on NaCl(2ML)/Cu(111) using different tip terminations. (a) Ag tip, $z = -0.7$ Å, $A = 0.6$ Å; (b) CO tip, $z = +1.3$ Å, $A = 0.7$ Å; (c) Cl tip, $z = -1.0$ Å, $A = 0.7$ Å; and (d) pentacene tip, $z = +0.6$ Å, $A = 0.5$ Å. The z values are given with respect to a STM set point of $I = 2$ pA, $V_b = 0.2$ V above the NaCl(2ML)/Cu(111) substrate. From ref. 17. Reprinted with permission from The American Association for the Advancement of Science.
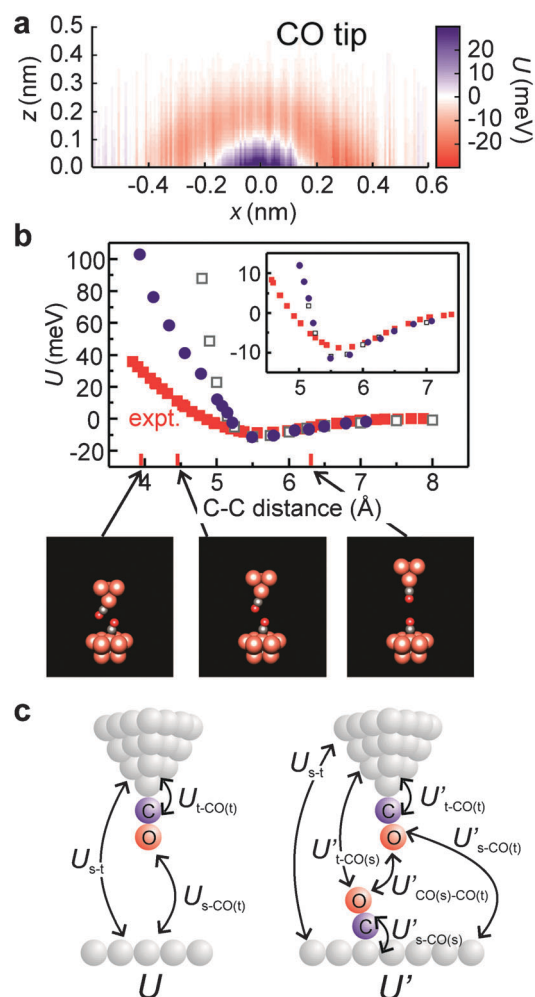
surrounding the molecule.[17,84] Therefore, atomic features only become visible when working at sufficiently small tip–sample distance, *i.e.* in the regime of Pauli repulsion between the tip and the surface. The chemical inertness of the CO molecule allows the tip to enter this regime without bonding to the molecule under investigation. In contrast, for less inert tips, *e.g.* Au, Ag, or Cu terminated tips, the attractive forces become too large, when approaching the molecule to enter the regime of Pauli repulsive forces, resulting in vertical or lateral manipulation of the molecule under investigation.[17]

While the qualitative benefits of the tip modification by, for example, a CO molecule are obvious, there are more subtle implications of molecule modified tips for force spectroscopy experiments. This can be illustrated by the study of the interaction between two CO molecules, one adsorbed at the AFM tip apex as explained above, and the other adsorbed on a single crystal metal substrate (here Cu(111)).[49] Fig. 5a shows the measured interaction energy at different tip–sample distances as a function of the lateral position ($x = 0$ corresponds to the position directly above the CO molecule on the substrate). Fig. 5b shows the interaction energy directly above the CO molecule as a function of the tip–sample distance (experimental data, filled red squares). Comparison with a DFT calculation for two fixed isolated CO molecules, *i.e.* neither the tip nor the substrate included in the calculations (open squares), shows quantitative agreement in the attractive regime (distance > 5.6 Å). However, the calculations overestimate the repulsive interaction at short tip–sample distances (distance < 5.3 Å). Including geometrical relaxations in the calculation (blue circles) improves the agreement between theory and experiment significantly.

What does the measured interaction energy correspond to in the repulsive regime where there is significant molecular reorientation? This is a long-standing problem in AFM with the realization that the tip structure and relaxation have to be considered to obtain a quantitative understanding of the force response.[24,85] For the experiment described above, the energy difference (ΔU) between a CO molecule adsorbed on the tip above a clean Cu(111) surface (U) and above a CO molecule adsorbed on the substrate (U') is measured (at a given tip–sample separation). The energy difference is given by (Fig. 5c):

$$\Delta U = U'_{\text{t-CO(s)}} + (U'_{\text{s-CO(s)}} - U_{\text{s-CO(s)}})$$
$$+ (U'_{\text{s-CO(t)}} - U_{\text{s-CO(t)}}) + (U'_{\text{t-CO(t)}} - U_{\text{t-CO(t)}})$$
$$+ U'_{\text{CO(s)-CO(t)}} \qquad (9)$$

where CO(t) and CO(s) refer to the CO molecule adsorbed on the tip and substrate. In the absence of molecular relaxation, all the terms in parenthesis are zero. A separate measurement of the interaction energy between a clean metal tip and the molecule on the substrate then allows extracting the intermolecular interaction based on purely experimental values. However, structural relaxation of the molecules causes the terms in parenthesis to be non-zero. The decreased repulsion between the CO molecules due to the geometric relaxation occurs at the expense of the adsorption energy terms ($U'_{\text{s-CO(s)}} - U_{\text{s-CO(s)}}$) and ($U'_{\text{t-CO(t)}} - U_{\text{t-CO(t)}}$). Finally, the problem with the $U'_{\text{t-CO(s)}}$ term is that it cannot be directly measured experimentally as it is the interaction between the tip and the relaxed CO geometry.

Fig. 5 (a) Experimental interaction energy over a CO molecule obtained by integration of vertical force data with a CO terminated tip. (b) Effect of relaxation on the force distance curves. The experimental background-corrected interaction energy directly above a CO molecule (filled red squares) compared with DFT calculation of two isolated CO molecules without geometry relaxation (open gray squares) and the full model that includes Cu_4 and Cu_{10} clusters as tip and substrate models, respectively, and where the CO molecules are allowed to relax (filled blue circles). Inset is a zoom-in into the attractive regime. The DFT energies correspond to the experimental situation, that is, the energy difference between a CO-modified tip approaching a bare metal substrate or an adsorbed CO molecule. The tip–sample distance in the experimental data has been shifted to overlay the vdW part of the interaction potential with the theoretical predictions. The lower images show the relaxed geometry at tip–substrate distances indicated by the arrows. (c) Schematics of the different interaction energy terms for the case of a CO-terminated tip on top of a clean metal substrate (left, term $U_{\text{s-CO(s)}}$ not indicated) and on top of an adsorbed CO molecule (right). Reproduced with permission from ref. 49. Copyright (2011) by the American Physical Society.

Selected examples

In the following section, various examples will be given illustrating how the concepts outlined above can be used to expand the capabilities of scanning probe methods. In the first section, the STM-directed synthesis of single molecules is discussed. In the section "Atomic scale structure determination

of organic molecules by AFM", the use of AFM to identify the structure of unknown molecules is presented. The topic of section "Kelvin probe force microscopy with sub-nanometre spatial resolution" is how Kelvin probe force microscopy (KPFM) can be used to identify the charge state of adsorbates.
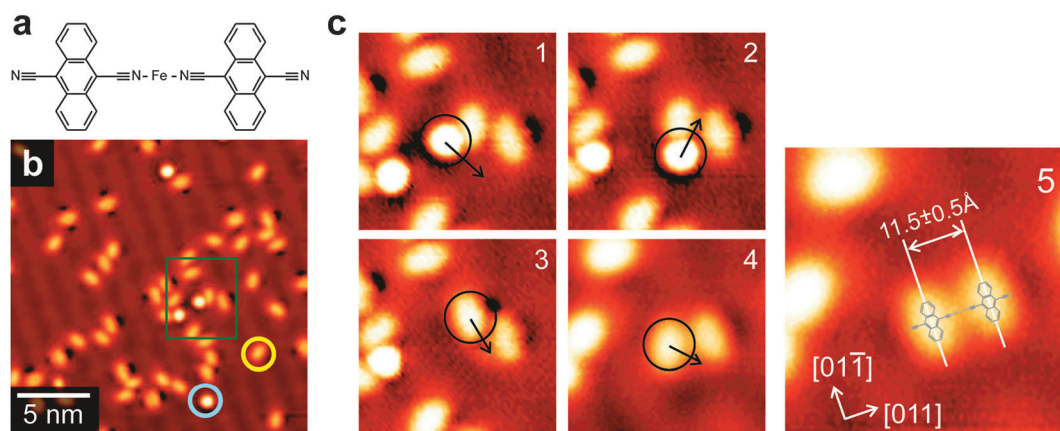
Single-molecule synthesis by STM

Controlled lateral manipulation of single atoms and molecules by scanning probe tips has made it possible to form artificial structures of atoms and molecules.[2,18,78,86,87] In addition, STM has been used to study chemical processes at the single molecule level.[18,20,81] The research has focused on reactions with increasing sophistication, starting from probing elementary reaction steps[4,78] on metal surfaces to visualizing changes that occur in the molecular orbitals during bond formation.[18]

On insulating films, traditional pushing and pulling methods that have been developed on metal surfaces to controllably laterally manipulate atoms and molecules cannot be applied. This is a consequence of the unfavourable diffusion barrier to binding energy ratio: it is relatively easy to pick up the molecule to be manipulated from the surface with the STM tip compared to successful lateral manipulation.[18,20] The problem can be partially alleviated by intentionally picking up a molecule onto the STM tip to reduce the probability of unintentional pickup of another molecule during manipulation. In addition, on ultrathin insulating films atoms and molecules can be laterally manipulated by vibrational excitation by inelastic electron tunnelling. While the yield of the manipulation process is not as high as on a metal surface, and directionality is hard to achieve, STM imaging can be used to reveal the exact adsorption geometry after the manipulation steps.
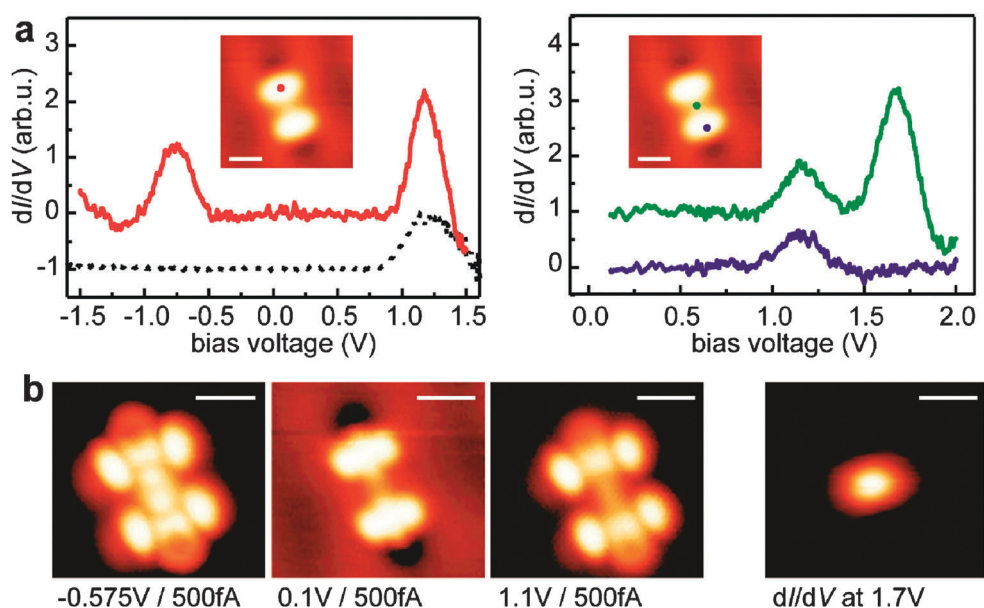
These techniques have been used to synthesize several covalently bonded metal–molecule complexes at the single molecule level.[18,20,81] Such studies provide access to structures that cannot easily be synthesized by standard organic chemistry techniques and which might exhibit useful functionality

in the framework of molecular electronics and spintronics. An example of a series of manipulation steps to form a metal–di-9,10-dicarbonitrile-anthracene complex $M(DCA)_2$ (structure shown in Fig. 6a) starting from individual atoms and dicarbonitrile-anthracene (DCA) molecules is shown in Figs. 6b and 6c.[20] After synthesis, the electronic coupling between the constituents is characterized by recording differential conductance spectra and by visualizing the orbitals of the complex (Fig. 7). As can be seen from the dI/dV_b spectra (Figs. 7a and 7b), the electronic structure of the $Fe(DCA)_2$ is qualitatively different from that of an isolated DCA ligand. Two additional resonances can be identified in the spectrum of the complex (at -0.8 V and at $+1.7$ V). The orbital images show that the first resonances at positive and negative bias are primarily derived from an orbital of the DCA ligand and are delocalized over the entire complex. In contrast, the second resonance at positive bias is a metal centred orbital (dI/dV_b image, Fig. 7b). The above conclusively proves that the two DCA molecules are electronically coupled via a metal bridge, i.e. that a covalently bonded metal–ligand complex has formed. By combining experimental observations (orbital ordering and symmetry) with DFT calculations, detailed information on the charge- and spin-state of the complex can be obtained. This approach indicates that the $Fe(DCA)_2$ complex is neutral and has 4 unpaired electrons.

The principle of single molecule synthesis by STM is general and can be extended to other molecules and metal atoms. For example, the synthesis of the $M(DCA)_2$ complex mentioned above was repeated using Ni instead of Fe atoms.[20] Also in this case there is covalent bonding between the constituents. However, the energetic position and the ordering of the orbitals are different from the iron complex. The formation reaction of these $M(DCA)_2$ complexes is not spontaneous. Simply bringing the reactants next to each other is not sufficient and inelastic excitation by the tunnelling electrons is necessary to overcome the activation energy barrier for the formation of the metal–ligand complex. The height of the activation barrier will depend on the forces between the two
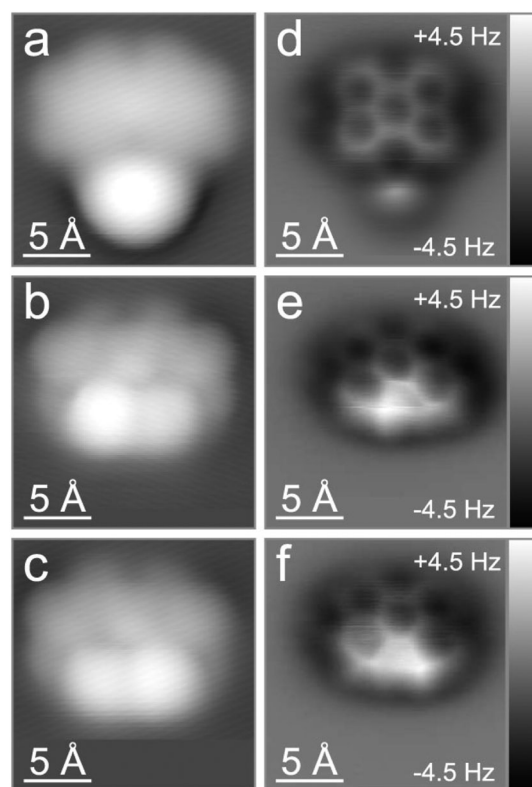

Fig. 6 Formation of a metal–ligand complex on an ultrathin insulating film by STM manipulation. (a) Structure of the target complex. (b) Large scale STM topography of DCA molecules (yellow circle) and iron atoms (blue circle) deposited on NaCl(2ML)/Cu(111). (c) Series of lateral manipulation steps resulting in the formation of a linear $Fe(DCA)_2$ complex (all images are 50×50 Å^2). Area corresponds to the area indicated by the green square in (b). Typical imaging parameters: $V_b = 0.1$ V and $I = 200$ fA. Adapted with permission from ref. 20. Copyright 2010 American Chemical Society.

Fig. 7 (a) Left panel: differential conductance spectra of an Fe(DCA)$_2$ complex (red solid line, acquired over one of the ligands, position indicated by the red dot in the inset) and an isolated DCA molecule (black dotted line). Right panel: spectra acquired at the centre (green) of the complex and over one of the ligands (blue). (b) Bias dependent imaging (left three images) and dI/dV_b image, showing the different spatial localization of the molecular orbitals. Adapted with permission from ref. 20. Copyright 2010 American Chemical Society.

reactants. For example, the barrier will be higher for two equally charged reactants compared to when one of them is neutral (or oppositely charged). The idea to control the barrier to bond formation *via* the charge-state can be exploited to form a molecular switch.[81] The switch is based on the reversible covalent bond formation between a negatively charged Au atom and a perylene-3,4,9,10-tetracarboxylic dianhydride (PTCDA) molecule. The current flowing through the complex differs by more than two orders of magnitude depending on the state of the switch (bonded *vs.* non-bonded). PTCDA molecules on NaCl(2ML)/Cu(111) are negatively charged. In addition, the charge state of single Au adatoms can be controlled on this surface by applying suitable voltage pulses.[22] Using a similar process as described above for the M(DCA)$_2$ complex, a negatively charged Au atom was moved close to a PTCDA$^-$ molecule (Fig. 8a). In this non-bonding configuration, atomically resolved AFM images show that the PTCDA molecule and Au atom are separate (Fig. 8d). At a sample bias of about -1.4 V (in the region of the PIR), electrons predominantly tunnel out of the singly occupied molecular orbital (SOMO) of the negatively charged PTCDA molecule, temporarily neutralizing the molecule.† This reduces the Coulomb repulsion between the Au$^-$ and PTCDA, which enables the adatom to change its position and form a bond with the molecule (Fig. 8b/c and 8e/f). At a sample bias of about $+1.4$ V (in the region of the NIR), electrons tunnel through a vacant orbital of the bonded singly negatively charged Au–PTCDA complex, temporarily adding an additional negative charge. This causes a Coulomb repulsion between the

Fig. 8 (a) STM image of an Au–PTCDA complex in the non-bonded configuration. (b) and (c) STM images corresponding to the two isomers of the bonded complex. Imaging parameters: $I = 3$ pA, $V_b = 0.2$ V. A CO terminated tip was used. (d)–(f) Corresponding constant-height AFM images. Imaging parameters: amplitude $A = 0.4$ Å, frequency $f_0 = 23\,165$ Hz and distance with respect to the STM set point above the substrate between 0.8 Å and 1.0 Å. Reproduced with permission from ref. 81. Copyright (2010) by the American Physical Society.

† The electronic decoupling of molecules adsorbed on an ultrathin NaCl layer leads to a significant increase in the lifetime of PIR and NIR states. If the state is sufficiently close to the Fermi-level, relaxations in the NaCl layer and the molecule can result in charge multi-stability.

adatom and the molecule, resulting in a breaking of the bond (Fig. 8a and d). Hence, the process of bond formation is completely reversible. The switching behaviour was found to be robust: a single complex could be switched several dozen times without any significant changes in behaviour.

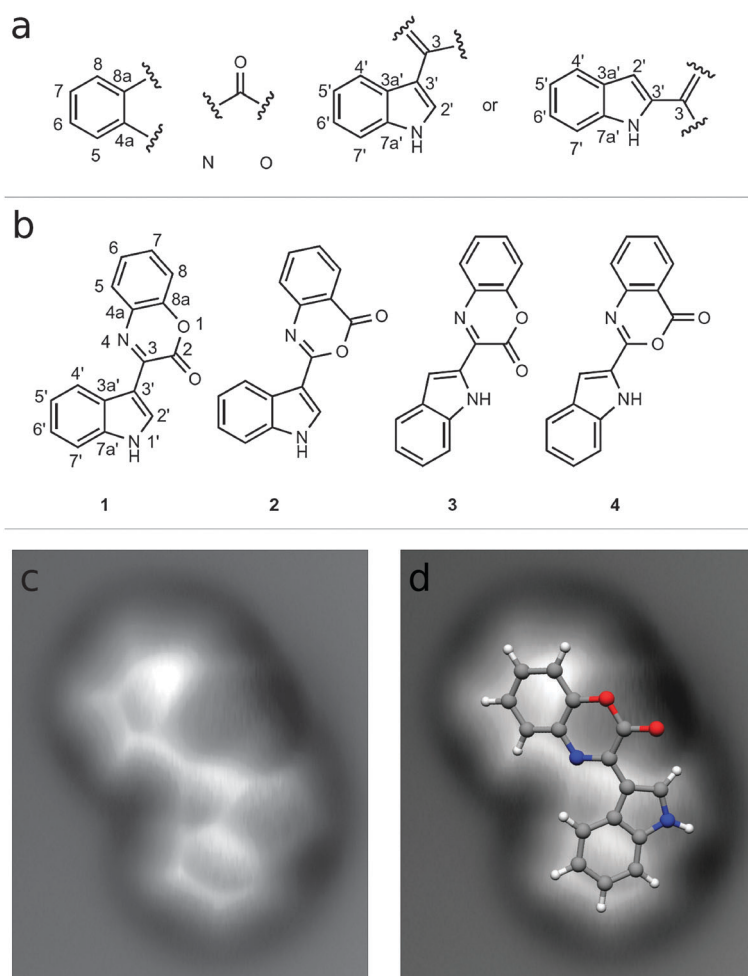### Atomic scale structure determination of organic molecules by AFM

Recently, imaging of individual molecules with atomic resolution by NC-AFM has proved to be useful in the identification of natural compounds.[80] Organic structure determination is important in the search for new medicines and standard tools for *ab initio* structural characterization include powerful techniques like nuclear magnetic resonance (NMR) and mass spectrometry (MS). However, even with these tools structural identification can be very challenging, particularly when using NMR methods on systems for which there is a limited number of protons, where the carbon skeleton is interrupted by heteroatoms, or where there are quaternary carbons that have no long-range correlations to protons.[88]

All these features are present in a metabolite of the pressure-tolerant actinobacterium *Dermacoccus abyssi*, which was isolated from the sediment collected from the deepest place on Earth, Challenger Deep in the Mariana Trench.[89] Using SPM in addition to NMR and MS, the molecule could be identified as cephalandole A,[80] a molecule that was originally found in a Taiwanese orchid and that was first misassigned[90] and later corrected.[91]

To identify the molecule from the deep sea bacterium, first its chemical formula was quickly determined to be $C_{16}H_{10}N_2O_2$ by high-resolution MS. Then state of the art NMR spectroscopy was carried out to determine the substructures (shown in Fig. 9a) and the connectivity of the molecule. However, the NMR results did not unambiguously resolve the structure, but left four possible working structures, displayed in Fig. 9b.

At this point NC-AFM measurements of the molecule were carried out. Molecules were adsorbed on a NaCl(2ML)/Cu(111) substrate and the AFM tip was functionalized with a CO molecule to achieve atomic resolution, as described above. The working structures shown in Fig. 9b could now be compared directly with the obtained AFM images. The placement of the indole bicycle was immediately clear, namely, on the lower right-hand side of the AFM image shown in

Fig. 9 Structure determination of cephalandole A. (a) Molecular fragments determined by NMR. (b) Possible working structures combining MS and NMR data. (c) NC-AFM image (amplitude $A = 0.5$ Å) using a CO functionalized tip. (d) NC-AFM image with structural model of cephalandole A superimposed. Reprinted by permission from Macmillan Publishers Ltd: Nature Chemistry ref. 80, copyright (2010).

Fig. 9c, where a six-membered ring connected to a five-membered ring is visible. Structures 3 and 4 could already be ruled out, because the angle between the two bicyclic systems could not be brought into accordance with the AFM measurements. This left only structure 1, cephalandole A, and structure 2, the previously misassigned structure of cephalandole A,[90] as candidates.

Finally, the determination of the adsorption site by SPM and comparison with DFT calculations ruled out structure 2 and unambiguously identified the molecule as structure 1, *i.e.* cephalandole A.[80] In Fig. 9d the structure of cephalandole A is superimposed on the AFM data, showing the excellent agreement between the structural model and the AFM image of the molecule.

The example shows that AFM can be a useful tool in structure determination of natural compounds where standard techniques are limited. Moreover, AFM offers the advantage of directly visualizing bonds, which is complementary to other techniques used for structure determination, and the ability to work with very small quantities of non-crystalline material. To become more powerful in the field of structure analysis, AFM could be advanced further towards chemical sensitivity on molecules as already demonstrated on semiconductor samples.[93] In a recent theoretical study it was indicated that comparing AFM data obtained with different tip terminations could be a possible route towards chemical identification on molecules.[94]

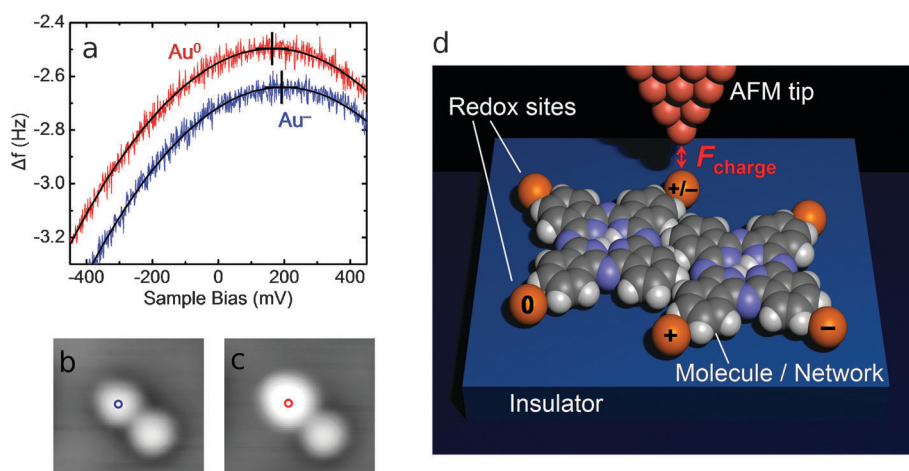### Kelvin probe force microscopy with sub-nanometre spatial resolution

An important extension of AFM is Kelvin probe force microscopy (KPFM).[95,96] In KPFM one measures the frequency shift Δf as a function of the bias voltage V_b applied between the tip and the sample. In general, Δf (and also the force F) is quadratically dependent on V_b, and when performing KPFM one determines the voltage V_{CPD} at the peak of the parabola (see section "Atomic force microscopy" and Fig. 10a). In the macroscopic case, CPD $= |e| \times V_{CPD}$ is the contact potential (work function) difference between the tip and the sample (where e is the electron charge). However, the signal also depends on the exact tip position on the atomic scale. Therefore, the measured quantity is named local contact potential difference (LCPD) with LCPD $= |e| \times V_{CPD}$. The lateral resolution of the LCPD obtained by KPFM has recently been pushed to the atomic scale.[16,97–102] With the ability to measure surface charges in the order of one electron, KPFM could become a very important tool for the investigation of molecular electronics, photonics, catalysis and photovoltaics. Atomic resolution KPFM with single electron charge sensitivity was demonstrated by measuring the different charge states of individual adatoms adsorbed on a thin insulating film, as described below.

It has been found that single gold atoms on NaCl(2ML)/ Cu(111) can be switched reversibly between neutral (Au^0) and negative (Au^-) charge states, by applying voltage pulses with the tip of an STM.[22] From DFT calculations it is known that the negative charge state (Au^-) is identified in STM images by a characteristic circular depression surrounding the adatom.[22,53] In comparison the neutral Au^0 atom shows no depression and a larger apparent height compared to Au^-, as can be seen in Fig. 10c.

Fig. 10a shows the voltage dependence of the frequency shift, measured with NC-AFM above Au^0 and Au^-. Both parabolas are measured without moving the tip between or during the measurements. To switch the charge state a bias voltage of $V_b = -1$ V has been applied for a few seconds in between measuring the two $\Delta f(V_b)$ parabolas. STM images taken before (Fig. 10b) and after (Fig. 10c) the $\Delta f(V_b)$ measurements confirm the switching from Au^- to Au^0.

When comparing the peaks of the two parabolas, we observe that on the one hand the peak position for Au^- is

Fig. 10 Charge switching of Au atoms. (a) Frequency shift Δf measured as a function of the sample voltage V_b above a gold atom, first charged negative (Au^-) and then neutral (Au^0). After measuring $\Delta f(V_b)$ above Au^-, the charge state is switched to Au^0 by applying a bias pulse of $V_b = -1$ V for a few seconds. Parabolic fits and corresponding parabola peaks are indicated. STM images ($I = 7.4$ pA, $V_b = -50$ mV, size 29 Å × 27 Å) before (b) and after (c) the $\Delta f(V_b)$ measurements (the position for the $\Delta f(V_b)$ measurements is indicated by circles) show the switched atom in the negative and neutral charge state, respectively. From ref. 16. Reprinted with permission from The American Association for the Advancement of Science. (d) Schematic setup of an experiment to study charge distributions and charge transport in molecular networks in a planar geometry. From ref. 92. Reprinted with permission from The American Association for the Advancement of Science.

shifted vertically towards a more negative Δf compared to Au^0. On the other hand, the Au^- peak is shifted horizontally towards a more positive V_{CPD} compared to Au^0. The former, *i.e.* the vertical shift of the parabola, is caused by the additional attractive electrostatic force above Au^- due to the attached electron. This increase in force could be quantified with the AFM and it amounts to 11 pN at a distance of 4.8 Å between the last atom of the tip (terminated with Au in this measurement) and the Au atom on the NaCl surface.[16,47]

The horizontal shift, *i.e.* the more positive LCPD measured above Au^- compared to Au^0, reflects the local increase of the work function. This increase stems from the surface dipole, directed from the vacuum to the surface, which is induced by the negative charge on the Au^- and its screening charge in the underlying substrate. Consistently, the LCPD shifts towards more negative values when an atom is charged positively, demonstrated for Ag^0 and Ag^+.[16,53] Using this technique the charge state of individual atoms can be determined by comparison of the LCPD.[16] Importantly this technique is applicable on insulators where STM cannot be performed and KPFM could be used to investigate single electron charge transport in molecular networks for future single electron devices[52,103] and molecular electronics.[104] For example, molecules could connect single atoms or small clusters, the latter acting as redox sites. By charging the redox sites with the tip, electrons can be injected into such a metal–molecular network, and their distribution and propagation in the network could be measured with KPFM as depicted in the schematic in Fig. 10d.

Conclusions and outlook

In this feature article, we have focused on recent developments in the field of single molecule chemistry with low-temperature STM and AFM. Key recent developments—STM experiments on ultrathin insulating films at low currents and the qPlus force sensor—have expanded the capabilities of the scanning probe microscopy toolbox such that we can start to explore the chemistry and physics of electronically isolated molecules at the single molecule level. Ultrathin insulating films grown on single crystal metals electronically decouple molecules from the substrate, allowing the electronic properties of unperturbed molecules to be studied. The qPlus force sensor allows non-contact AFM experiments to be performed with sub-Ångström oscillation amplitudes. As a consequence, the force detection is predominantly sensitive to short-range chemical forces, providing atomic contrast in AFM imaging of single molecules. In addition to the examples that were reviewed, these techniques open up a wealth of opportunities for other experiments. They could be combined with other important developments in the rapidly developing field of scanning probe microscopy, such as dynamical STM studies with picosecond time resolution and spin sensitivity in electron tunnelling and force detection.[105–107] Another exciting possibility is to combine the high spatial resolution of the AFM with charge detection to quantify the charge distribution in single molecules and molecular assemblies. Together with atomic manipulation, this can open a way for STM and AFM experiments on artificially engineered molecular assemblies on insulators to study single electron transport and chemical reactions of relevance in chemistry, biochemistry and physics.

Notes and references

1 G. Binnig, H. Rohrer, C. Gerber and E. Weibel, *Phys. Rev. Lett.*, 1983, **50**, 120.
2 D. M. Eigler and E. K. Schweizer, *Nature*, 1990, **344**, 524.
3 B. C. Stipe, M. A. Rezaei and W. Ho, *Science*, 1998, **280**, 1732.
4 H. J. Lee and W. Ho, *Science*, 1999, **286**, 1719.
5 F. J. Giessibl, S. Hembacher, H. Bielefeldt and J. Mannhart, *Science*, 2000, **289**, 422.
6 G. V. Nazin, X. H. Qiu and W. Ho, *Science*, 2003, **302**, 77.
7 M. Ashino, A. Schwarz, T. Behnke and R. Wiesendanger, *Phys. Rev. Lett.*, 2004, **93**, 136101.
8 J. Repp, G. Meyer, S. M. Stojković, A. Gourdon and C. Joachim, *Phys. Rev. Lett.*, 2005, **94**, 026803.
9 C. F. Hirjibehedin, C. P. Lutz and A. J. Heinrich, *Science*, 2006, **312**, 1021.
10 B. J. Albers, T. C. Schwendemann, M. Z. Baykara, N. Pilet, M. Liebmann, E. I. Altman and U. D. Schwarz, *Nat. Nanotechnol.*, 2009, **4**, 307.
11 R. Temirov, S. Soubatch, O. Neucheva, A. C. Lassise and F. S. Tautz, *New J. Phys.*, 2008, **10**, 053012.
12 C. Weiss, C. Wagner, C. Kleimann, M. Rohlfing, F. S. Tautz and R. Temirov, *Phys. Rev. Lett.*, 2010, **105**, 086103.
13 C. Weiss, C. Wagner, R. Temirov and F. S. Tautz, *J. Am. Chem. Soc.*, 2010, **132**, 11864.
14 F. J. Giessibl, *Rev. Mod. Phys.*, 2003, **75**, 949.
15 *Noncontact Atomic Force Microscopy*, ed. S. Morita, F. J. Giessibl and R. Wiesendanger, Springer, Berlin, 2009, vol. 2.
16 L. Gross, F. Mohn, P. Liljeroth, J. Repp, F. J. Giessibl and G. Meyer, *Science*, 2009, **324**, 1428.
17 L. Gross, F. Mohn, N. Moll, P. Liljeroth and G. Meyer, *Science*, 2009, **325**, 1110.
18 J. Repp, G. Meyer, S. Paavilainen, F. E. Olsson and M. Persson, *Science*, 2006, **312**, 1196.
19 P. Liljeroth, J. Repp and G. Meyer, *Science*, 2007, **317**, 1203.
20 P. Liljeroth, I. Swart, S. Paavilainen, J. Repp and G. Meyer, *Nano Lett.*, 2010, **10**, 2475.
21 J. Repp and G. Meyer, *Appl. Phys. A: Solid Surf.*, 2006, **85**, 399.
22 J. Repp, G. Meyer, F. E. Olsson and M. Persson, *Science*, 2004, **305**, 493.
23 J. Tersoff and D. R. Hamann, *Phys. Rev. B*, 1985, **31**, 805.
24 W. A. Hofer, A. S. Foster and A. L. Shluger, *Rev. Mod. Phys.*, 2003, **75**, 1287.
25 R. M. Feenstra, *Surf. Sci.*, 1994, **299–300**, 965.
26 C. Wittneven, R. Dombrowski, M. Morgenstern and R. Wiesendanger, *Phys. Rev. Lett.*, 1998, **81**, 5616.
27 M. Passoni, F. Donati, A. Li Bassi, C. S. Casari and C. E. Bottani, *Phys. Rev. B: Condens. Matter Mater. Phys.*, 2009, **79**, 045404.
28 B. Koslowski, H. Pfeifer and P. Ziemann, *Phys. Rev. B: Condens. Matter Mater. Phys.*, 2009, **80**, 165419.
29 M. Ziegler, N. Néel, A. Sperl, J. Kröger and R. Berndt, *Phys. Rev. B: Condens. Matter Mater. Phys.*, 2009, **80**, 125402.
30 C. W. J. Beenakker, *Phys. Rev. B: Condens. Matter*, 1991, **44**, 1646.
31 L. J. Lauhon and W. Ho, *Rev. Sci. Instrum.*, 2001, **72**, 216.

32 J. Repp, G. Meyer, S. Paavilainen, F. E. Olsson and M. Persson, *Phys. Rev. Lett.*, 2005, **95**, 225503.

33 S. W. Wu, G. V. Nazin, X. Chen, X. H. Qiu and W. Ho, *Phys. Rev. Lett.*, 2004, **93**, 236802.

34 I. Swart, T. Sonnleitner and J. Repp, *Nano Lett.*, 2011, **11**, 1580.

35 B. J. LeRoy, S. G. Lemay, J. Kong and C. Dekker, *Nature*, 2004, **432**, 371.

36 Z. Sun, I. Swart, C. Delerue, D. Vanmaekelbergh and P. Liljeroth, *Phys. Rev. Lett.*, 2009, **102**, 196401.

37 X. H. Qiu, G. V. Nazin and W. Ho, *Phys. Rev. Lett.*, 2004, **92**, 206102.

38 N. Ogawa, G. Mikaelian and W. Ho, *Phys. Rev. Lett.*, 2007, **98**, 166103.

39 J. Repp, P. Liljeroth and G. Meyer, *Nat. Phys.*, 2010, **6**, 975.

40 B. C. Stipe, M. A. Rezaei and W. Ho, *Science*, 1998, **279**, 1907.

41 K. Morgenstern, *Acc. Chem. Res.*, 2009, **42**, 213.

42 R. Stomp, Y. Miyahara, S. Schaer, Q. Sun, H. Guo, P. Grutter, S. Studenikin, P. Poole and A. Sachrajda, *Phys. Rev. Lett.*, 2005, **94**, 056802.

43 F. J. Giessibl and C. F. Quate, *Phys. Today*, 2006, **59**, 44.

44 M. Ternes, C. P. Lutz, C. F. Hirjibehedin, F. J. Giessibl and A. J. Heinrich, *Science*, 2008, **319**, 1066.

45 F. J. Giessibl, *Phys. Rev. B: Condens. Matter*, 1997, **56**, 16010.

46 F. J. Giessibl, *Appl. Phys. Lett.*, 2001, **78**, 123.

47 J. E. Sader and S. P. Jarvis, *Appl. Phys. Lett.*, 2004, **84**, 1801.

48 H. Hölscher, U. D. Schwarz and R. Wiesendanger, *Appl. Surf. Sci.*, 1999, **140**, 344.

49 Z. Sun, M. P. Boneschanscher, I. Swart, D. Vanmaekelbergh and P. Liljeroth, *Phys. Rev. Lett.*, 2011, **106**, 046104.

50 U. Kaiser, A. Schwarz and R. Wiesendanger, *Nature*, 2007, **446**, 522.

51 Y. Azuma, M. Kanehara, T. Teranishi and Y. Majima, *Phys. Rev. Lett.*, 2006, **96**, 016108.

52 K. Uchida, in *Nanoelectronics and Information Technology: Advanced Electronic Materials and Novel Devices*, ed. R. Waser, Wiley, New York, 2003.

53 F. E. Olsson, S. Paavilainen, M. Persson, J. Repp and G. Meyer, *Phys. Rev. Lett.*, 2007, **98**, 176803.

54 S. W. Wu, N. Ogawa, G. V. Nazin and W. Ho, *J. Phys. Chem. C*, 2008, **112**, 5451.

55 C. Chen, P. Chu, C. A. Bobisch, D. L. Mills and W. Ho, *Phys. Rev. Lett.*, 2010, **105**, 217402.

56 A. J. Heinrich, J. A. Gupta, C. P. Lutz and D. M. Eigler, *Science*, 2004, **306**, 466.

57 Y.-S. Fu, T. Zhang, S.-H. Ji, X. Chen, X.-C. Ma, J.-F. Jia and Q.-K. Xue, *Phys. Rev. Lett.*, 2009, **103**, 257202.

58 S. Loth, K. von Bergmann, M. Ternes, A. F. Otte, C. P. Lutz and A. J. Heinrich, *Nat. Phys.*, 2010, **6**, 340.

59 S. Schintke, S. Messerli, M. Pivetta, F. Patthey, L. Libioulle, M. Stengel, A. De Vita and W.-D. Schneider, *Phys. Rev. Lett.*, 2001, **87**, 276801.

60 G. Kresse, M. Schmid, E. Napetschnig, M. Shishkin, L. Köhler and P. Varga, *Science*, 2005, **308**, 1440.

61 R. Bennewitz, V. Barwich, M. Bammerlin, C. Loppacher, R. Guggisberg, A. Baratoff, E. Meyer and H. J. Güntherodt, *Surf. Sci.*, 1999, **438**, 289.

62 S. Fölsch, A. Helms, S. Zöphel, J. Repp, G. Meyer and K. H. Rieder, *Phys. Rev. Lett.*, 2000, **84**, 123.

63 J. Repp, S. Fölsch, G. Meyer and K.-H. Rieder, *Phys. Rev. Lett.*, 2001, **86**, 252.

64 F. E. Olsson, M. Persson, J. Repp and G. Meyer, *Phys. Rev. B: Condens. Matter Mater. Phys.*, 2005, **71**, 075419.

65 W. Hebenstreit, J. Redinger, Z. Horozova, M. Schmid, R. Podloucky and P. Varga, *Surf. Sci.*, 1999, **424**, L321.

66 K. Glöckler, M. Sokolowski, A. Soukopp and E. Umbach, *Phys. Rev. B: Condens. Matter*, 1996, **54**, 7705.

67 S. Fölsch, *Elektronenspektroskopische Untersuchungen zur H₂O-Adsorption auf der NaCl(100)-Oberfläche*, PhD thesis, University of Hannover, Hannover, 1991.

68 L. Bartels, G. Meyer and K. H. Rieder, *Phys. Rev. Lett.*, 1997, **79**, 697.

69 T. A. Jung, R. R. Schlittler, J. K. Gimzewski, H. Tang and C. Joachim, *Science*, 1996, **271**, 181.

70 F. Moresco, L. Gross, M. Alemani, K.-H. Rieder, H. Tang, A. Gourdon and C. Joachim, *Phys. Rev. Lett.*, 2003, **91**, 036601.

71 D. L. Keeling, M. J. Humphry, R. H. J. Fawcett, P. H. Beton, C. Hobbs and L. Kantorovich, *Phys. Rev. Lett.*, 2005, **94**, 146104.

72 L. Grill, *J. Phys.: Condens. Matter*, 2008, **20**, 053001.

73 F. Moresco, G. Meyer, K.-H. Rieder, H. Tang, A. Gourdon and C. Joachim, *Phys. Rev. Lett.*, 2001, **87**, 088302.

74 D. M. Eigler, C. P. Lutz and W. E. Rudge, *Nature*, 1991, **352**, 600.

75 L. Bartels, G. Meyer and K. H. Rieder, *Appl. Phys. Lett.*, 1997, **71**, 213.

76 L. Lafferentz, F. Ample, H. Yu, S. Hecht, C. Joachim and L. Grill, *Science*, 2009, **323**, 1193.

77 N. Néel, J. Kröger, L. Limot, T. Frederiksen, M. Brandbyge and R. Berndt, *Phys. Rev. Lett.*, 2007, **98**, 065502.

78 S. W. Hla, L. Bartels, G. Meyer and K. H. Rieder, *Phys. Rev. Lett.*, 2000, **85**, 2777.

79 W. Ho, *J. Chem. Phys.*, 2002, **117**, 11033.

80 L. Gross, F. Mohn, N. Moll, G. Meyer, R. Ebel, W. M. Abdel-Mageed and M. Jaspars, *Nat. Chem.*, 2010, **2**, 821.

81 F. Mohn, J. Repp, L. Gross, G. Meyer, M. S. Dyer and M. Persson, *Phys. Rev. Lett.*, 2010, **105**, 266102.

82 Y. Sugimoto, M. Abe, S. Hirayama, N. Oyabu, O. Custance and S. Morita, *Nat. Mater.*, 2005, **4**, 156.

83 Y. Sugimoto, P. Pou, O. Custance, P. Jelinek, M. Abe, R. Perez and S. Morita, *Science*, 2008, **322**, 413.

84 N. Moll, L. Gross, F. Mohn, A. Curioni and G. Meyer, *New J. Phys.*, 2010, **12**, 125020.

85 L. N. Kantorovich and T. Trevethan, *Phys. Rev. Lett.*, 2004, **93**, 236102.

86 M. F. Crommie, C. P. Lutz and D. M. Eigler, *Science*, 1993, **262**, 218.

87 A. J. Heinrich, C. P. Lutz, J. A. Gupta and D. M. Eigler, *Science*, 2002, **298**, 1381.

88 P. Crews, J. Rodriguez and M. Jaspars, *Organic Structure Analysis*, Oxford University Press, Oxford, 2010.

89 W. Pathom-Aree, J. E. M. Stach, A. C. Ward, K. Horikoshi, A. T. Bull and M. Goodfellow, *Extremophiles*, 2006, **10**, 181.

90 P. L. Wu, Y. L. Hsu and C. W. Jao, *J. Nat. Prod.*, 2006, **69**, 1467.

91 J. J. Mason, J. Bergman and T. Janosik, *J. Nat. Prod.*, 2008, **71**, 1447.

92 E. Meyer and T. Glatzel, *Science*, 2009, **324**, 1397.

93 Y. Sugimoto, P. Pou, M. Abe, P. Jelinek, R. Perez, S. Morita and O. Custance, *Nature*, 2007, **446**, 64.

94 C.-S. Guo, M. A. Van Hove, R.-Q. Zhang and C. Minot, *Langmuir*, 2010, **26**, 16271.

95 J. M. R. Weaver and D. W. Abraham, *J. Vac. Sci. Technol., B*, 1991, **9**, 1559.

96 M. Nonnenmacher, M. P. O'Boyle and H. K. Wickramasinghe, *Appl. Phys. Lett.*, 1991, **58**, 2921.

97 T. Eguchi, Y. Fujikawa, K. Akiyama, T. An, M. Ono, T. Hashimoto, Y. Morikawa, K. Terakura, T. Sakurai, M. G. Lagally and Y. Hasegawa, *Phys. Rev. Lett.*, 2004, **93**, 266102.

98 F. Bocquet, L. Nony, C. Loppacher and T. Glatzel, *Phys. Rev. B: Condens. Matter Mater. Phys.*, 2008, **78**, 035410.

99 G. H. Enevoldsen, T. Glatzel, M. C. Christensen, J. V. Lauritsen and F. Besenbacher, *Phys. Rev. Lett.*, 2008, **100**, 236104.

100 S. Sadewasser, P. Jelinek, C.-K. Fang, O. Custance, Y. Yamada, Y. Sugimoto, M. Abe and S. Morita, *Phys. Rev. Lett.*, 2009, **103**, 266103.

101 Y. Sugawara, T. Uchihashi, M. Abe and S. Morita, *Appl. Surf. Sci.*, 1999, **140**, 371.

102 F. Bocquet, L. Nony and C. Loppacher, *Phys. Rev. B: Condens. Matter Mater. Phys.*, 2011, **83**, 035411.

103 K. K. Likharev, *Proc. IEEE*, 1999, **87**, 606.

104 C. Joachim, J. K. Gimzewski and A. Aviram, *Nature*, 2000, **408**, 541.

105 S. Loth, M. Etzkorn, C. P. Lutz, D. M. Eigler and A. J. Heinrich, *Science*, 2010, **329**, 1628.

106 J. Brede, N. Atodiresei, S. Kuck, P. Lazić, V. Caciuc, Y. Morikawa, G. Hoffmann, S. Blügel and R. Wiesendanger, *Phys. Rev. Lett.*, 2010, **105**, 047204.

107 R. Wiesendanger, *Rev. Mod. Phys.*, 2009, **81**, 1495.